High Resolution Coherent Doppler Wind Lidar Incorporating Phase-Shift Keying

Yunpeng Zhang, Yunbin Wu, Haiyun Xia

***Abstract*—A coherent Doppler wind lidar (CDWL) with spatial/temporal resolution of meter and sub-second scale is reported. Phase-shift keying (PSK) is introduced into the pulse pair to enhance the measurement efficiency, and the pulse shaping and perfect binary PSK modulation are both realized by a single Mach-Zehnder modulator (MZM). The identical intensity envelope of the paired pulses reduces the influence of amplifier's gain profile and provides a monitoring parameter for bias control, which improves the system stability in practice. Theoretical analysis and numerical simulation are conducted to illustrate the principle of the proposed method. In experiments, the bias drift of the MZM is monitored in real time. Continuous radial wind profile measurement over 800 m is demonstrated with spatial and temporal resolution of 3 m and 0.1 s, respectively.**

***Index Terms*—coherent Doppler lidar, phase-shift keying, spatial resolution, differential correlation pair.**

I. Introduction

As a powerful remote sensing technique, Doppler wind lidar has been widely used in scientific researches and engineering applications, such as gravity waves monitoring [1],[2], boundary layer detection [3],[4], wind energy exploitation [5],[6], weather forecast [7], and air pollution analysis [8],[9]. Due to the inherent properties of coherent detection, a coherent Doppler wind lidar (CDWL) has the advantage of acquiring the spectral characteristics of the atmospheric backscattered signals, which extends its scope to spectrum analysis based applications like precipitation observation [10],[11], cloud phase identification [12] and so on.

Despite all these successful examples, the performance of CDWLs still needs to be further improved in some aspects. In areas like aerodynamics design and aviation safety, the CDWL has been used to detect the aircraft wake vortices [13],[14]. Since the wingspan of the aircraft is on the order of ten meters, meter-scale detection of the wind field raises higher requirements for the CDWL. With higher spatial/temporal resolution, more detailed data can be got in the field experiment, thus improving the estimation accuracy of the wake vortex parameters [15],[16].

Nevertheless, it's quite challenging to enhance the spatial resolution of a conventional pulsed CDWL to meter scale, which depends on the pulse duration [17]. When the pulse duration is shortened to tens of nanoseconds, the estimation accuracy of the Doppler frequency shift will be greatly degraded due to the spectrum broadening of the backscattered signals [18]. Moreover, the limited peak power of fiber lasers further aggravates the carrier-to-noise ratio (CNR) of the backscattered signal under short pulse duration [19]. To mitigate these negative effects, complicated hardware and algorithms have to be adopted under conventional pulsed method, realizing the spatial resolutions from 3 m to 60 m [20-22]. Recently, several works are reported to enhance the spatial resolution without shortening the pulse duration. In the pseudo-random phase coding (PRPC) method [23], a 4.5-m spatial resolution is realized by decoupling the spatial resolution and pulse duration with the pseudo-random phase modulation of the lightwave. However, to achieve the fast phase transition between bits, a very high modulation bandwidth is required. Another attempt is the differential correlation pair (DCP) method [24], where the spatial resolution is determined by the duration of the short probing pulse and the window function. Under this scheme, the spatial resolution is enhanced to 3.3 m. However, due to the different intensity envelopes of the paired pulses, the pulse shape before amplification needs to be particularly designed to adapt to the gain characteristics of the amplifier, so as to ensure the cancellation of the common pulses.

In this work, we propose and demonstrate a novel CDWL incorporating the DCP technique and phase-shift keying (PSK) modulation. Inspired by the phase-shift pulse technique in distributed fiber sensors [25], the proposed PSK-DCP method adopts probing pulses with phase difference of π, thus enhancing the measurement efficiency compared with the original DCP scheme. Since the phase modulation does not change the intensity envelope, the influence of the amplifier's gain profile can be greatly reduced when the pulses are equally spaced, which makes the system more robust to environmental disturbance. To facilitate engineering applications, the PSK modulation together with the pulse shaping is realized by a single Mach-Zehnder modulator (MZM) [26]. Meanwhile, a real-time bias monitoring scheme for the MZM is proposed.

Manuscript received ; revised ; accepted . Date of publication ; date of current version . This work was supported by the National Ten Thousand Talent Program in China and Strategic Priority Research Program of Chinese Academy of Sciences under Grant No. XDA22040601. (*Corresponding author: Haiyun Xia*.)

Yunpeng Zhang, Yunbin Wu and Haiyun Xia are with School of Earth and Space Sciences, University of Science and Technology of China (USTC), Hefei 230026, China. (e-mail: zyp110@mail.ustc.edu.cn; wuyunbin@mail.ustc.edu.cn; hsia@ustc.edu.cn;).

Haiyun Xia is also with School of Atmospheric Physics, Nanjing University of Information Science and Technology, Nanjing 210044, China; Hefei National Laboratory for Physical Sciences at the Microscale, USTC, Hefei 230026, China; and Institute of Software, Chinese Academy of Sciences, Beijing 100190, China.

Color versions of one or more of the figures in this article are available online at https://ieeexplore.ieee.org.

Digital Object Identifier

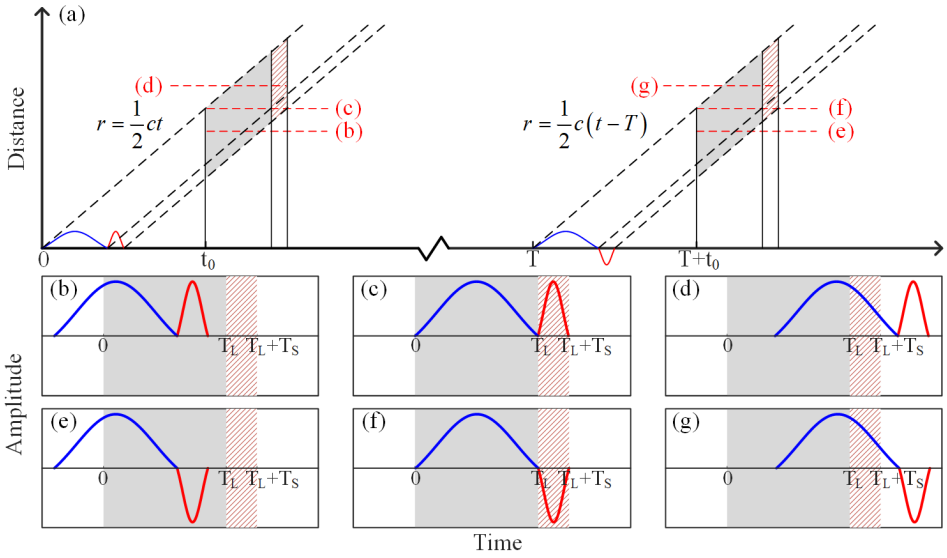

Fig. 1. Principle of the PSK-DCP lidar. The common and probing pulses are colored by blue and red, while the long and short windows are shaded by gray and pink grid, respectively. (a) Schematic diagram of the contribution of signals from different distances. (b)-(d) Backscattered signals of the odd pulse from different distances. (e)-(g) Backscattered signals of the even pulse from different distances.

II. Principle

A. CDWL with Phase-Shift Keying

In the DCP method, the transmitted pulses' amplitude envelopes are composed of a long common pulse $A_L(t)$ and a followed short probing pulse $A_S(t)$ with truncation lengths of T_L and T_S, respectively [24]. When binary PSK is employed, the probing pulse in the even pulse is phase shifted by π. It is noted that the phase shift is defined by the phase difference between the common pulse and probing pulse in the even pulse, rather than the odd and even pulses. As illustrated in Fig. 1, the amplitude envelopes of the *i*th (*i*=1,2) pulse in the pair can be expressed by:

$$A^{(i)}(t)=A_L(t)+(-1)^{i-1}\cdot A_S(t) \tag{1}$$

According to the classical layered model of atmospheric scattering [27], the backscattered signal can be modeled as the superposition of the random atmospheric reflections from different slices. Provided the pulse duration is less than the relaxation time of the scattering particles, only little phase distortion would be introduced in the scattering [27]. After heterodyne detection, the received signal is:

$$r^{(i)}(t)=\int A^{(i)}\left(t-\frac{2z}{c}\right)\kappa(z)\exp\left\{j2\pi\left[f_{IF}+f_d(z)\right]t\right\}dz \tag{2}$$

where $f_{IF}=f_c-f_{LO}$ is the intermediate frequency (IF) with f_c and f_{LO} being the frequency of carrier and local oscillator, $f_d(z)$ is the Doppler frequency shift caused by the motion of aerosols, c is the speed of light in the atmosphere, and $\kappa(z)$ is a circular random variable representing the random scattering feature of the atmosphere. Constants are omitted from the equation for brevity.

To retrieve the wind velocity at distance $z_0=ct_0/2$, a long window function $W_L(t-t_0)$ and a short window function $W_S(t-t_0)$ are used to truncate the received IF signal. The truncation lengths of the two window functions are the same as the common pulse and probing pulse, respectively. The windowed IF signals are denoted by $r_L^{(i)}(t,t_0)$ and $r_S^{(i)}(t,t_0)$, respectively. Substituting (2), their cross-correlation $R^{(i)}(\tau,t_0)$ is calculated as:

$$\begin{aligned}R^{(i)}(\tau,t_0)&=\left\langle\int r_L^{(i)}(t',t_0)\overline{r_S^{(i)}(t'+\tau,t_0)}dt'\right\rangle\\&=\int\left\langle r^{(i)}(t')\overline{r^{(i)}(t'+\tau)}\right\rangle W_L(t'-t_0)W_s(t'+\tau-t_0)dt'\\&=\iiint\exp\left\{j2\pi\left[f_d(z)t-f_d(z')(t'+\tau)-f_{IF}\tau\right]\right\}\times\\&\quad\left\langle\kappa(z)\overline{\kappa(z')}\right\rangle A^{(i)}\left(t'-\frac{2z}{c}\right)A^{(i)}\left(t'+\tau-\frac{2z'}{c}\right)\times\\&\quad W_L(t'-t_0)W_s(t'+\tau-t_0)dz'dzdt'\end{aligned} \tag{3}$$

where the operation $\langle\bullet\rangle$ refers to averaging over pulses and $\overline{\bullet}$ refers to complex conjugate. Due to the random nature of aerosol scatters, the auto-correlation of $\kappa(z)$ is $\beta(z)\delta(z-z')$, with $\beta(z)$ being the mean reflectivity at distance z and $\delta(z-z')$ being the Dirac delta function. By defining $z=z_0+\delta z$ and $t=t'-t_0$ with $z_0=ct_0/2$ and $\delta z=c\delta t/2$, the $R^{(i)}(\tau,t_0)$ can be simplified as:

$$\begin{aligned}R^{(i)}(\tau,t_0)&=\iiint\exp\left\{j2\pi\left[f_d(z)t-f_d(z')(t'+\tau)-f_{IF}\tau\right]\right\}\times\\&\beta(z)\delta(z-z')A^{(i)}\left(t'-\frac{2z}{c}\right)A^{(i)}\left(t'+\tau-\frac{2z'}{c}\right)\times\\&W_L(t'-t_0)W_s(t'+\tau-t_0)dz'dzdt'\\&=\int\beta(z)\exp\left\{-j2\pi\left[f_{IF}+f_d(z)\right]\tau\right\}dz\times\\&\int A^{(i)}(t-\delta t)A^{(i)}(t-\delta t+\tau)W_L(t)W_s(t+\tau)dt\\&=\int\beta(z_0+\delta z)\sum_{a,b}(-1)^{(a-b)(i-1)}F_{ab}(\delta z,\tau)\times\\&\exp\left\{-j2\pi\left[f_{IF}+f_d(z_0+\delta z)\right]\tau\right\}d(\delta z)\end{aligned}\tag{4}$$

where $F_{ab}=\int A_a(t-\delta t)A_b(t-\delta t+\tau)W_L(t)W_S(t+\tau)dt$ with a,b in the range of *"L"* and *"S"*.

The contribution of F_{ab} can be explicitly analyzed with the help of Fig. 1. Firstly, F_{SL} is zero for all the cases. When $\delta t<0$ (Fig. 1(b, e)), $A_S(t-\delta t)W_L(t)\neq 0$ but only when $\delta t>0$ (Fig. 1(d, g)), $A_L(t+\tau-\delta t)W_S(t+\tau)\neq 0$, which makes their product always zero. Secondly, since the F_{LL} and F_{SS} terms exist in both $R^{(1)}(\tau,t_0)$ and $R^{(2)}(\tau,t_0)$, they will be eliminated in a differential operation. Thus, only the F_{LS} term remains in the differential cross-correlation (Fig. 1(c, f)), leading to:

$$\begin{aligned}R_d(\tau,t_0)&=R^{(1)}(\tau,t_0)-R^{(2)}(\tau,t_0)\\&=\int 2\beta(z_0+\delta z)F_{LS}(\delta z,\tau)\times\\&\exp\left\{-j2\pi\left[f_{IF}+f_d(z_0+\delta z)\right]\tau\right\}d(\delta z)\end{aligned}\tag{5}$$

To further understand the characteristics of the F_{LS}, a numerical simulation is carried out. The window functions and the pulses' amplitude envelopes are set to be truncated Gaussian functions, where the half width at exp(-0.5) and truncated length of both W_L and A_L are 52 ns and 200 ns, while those parameters of W_S and A_S are 8 ns and 30 ns. The parameters are chosen for imitating the behavior of the experiment system described in Section III.

The contour map of the F_{LS} is shown in Fig. 2(a) with its sections cut at τ=115 ns and $\delta t=0$ shown in Fig. 2 (b) and (c). The variations of the F_{LS} in the τ and δt axes indicate the amplitude changes of the signal scattered by a specific spatial slice and the different contributions of the signals originate from different spatial slices, respectively. It can be observed that the non-zero part along the δt axis is determined by the duration of the short probing pulse while the non-zero part along the τ axis is mainly determined by the long common pulse. Note that $\delta t=2\delta z/c$, the Eq. (5) indicates that the spatial resolution and the effective duration of the $R_d(\tau,t_0)$ for a specific t_0 depend on the probing pulse and common pulse, respectively. Thus, by substituting the parameters of the probing pulse and the short window function, the recognized formula of the pulsed CDWL's spatial resolution can still hold, specifically [17]:

$$\Delta z=\frac{1}{2}c\left[\pi\left(\sigma_p^2+\sigma_w^2\right)\right]^{0.5}\tag{6}$$

where σ_p and σ_w are the half width at exp(-0.5) of the probing pulse's amplitude envelope and the Gaussian window function, respectively. More detailed information about the simulation can be found in the Appendix.

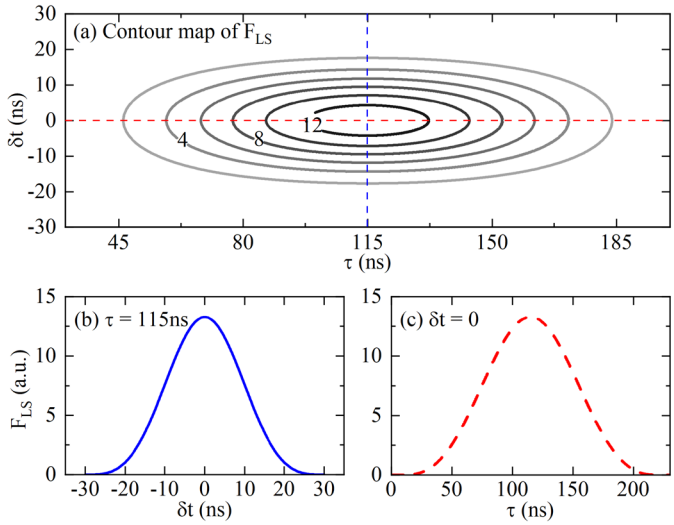

Fig. 2. (a) Contour map of the F_{LS} in simulation and its sections cut at (b) τ=115 ns and (c) δt=0

B. PSK Modulation and Bias Monitoring Based on MZM

Typically, the intensity and phase modulation can be realized by an MZM and a phase modulator (PM), respectively. However, an additional phase modulator will increase the complexity and decrease the robustness of the system, as the half-wave voltages of both the MZM and PM need to be calibrated. To avoid that, we employ a single MZM biased at the null point to realize pulse shaping and binary PSK modulation here. Meanwhile, the bias of the MZM can be monitored in real time from the modulated intensity waveform. The transfer function of an MZM can be expressed as [26]:

$$h\left[V_m(t)\right]=\exp(j\phi_0)\cos\left[\frac{\pi}{2}\frac{V_m(t)}{V_{\pi\mathrm{RF}}}+\frac{\pi}{2}\frac{V_{DC}}{V_{\pi\mathrm{DC}}}\right]\tag{7}$$

where $V_m(t)$ is the modulation voltage, V_{DC} is the DC offset, $V_{\pi\mathrm{RF}}$ and $V_{\pi\mathrm{DC}}$ are the half-wave voltages of the RF and DC electrodes, and ϕ_0 is the common phase shift introduced by the modulator. For simplicity, the ϕ_0 can be set to π without losing generality. When the modulator is biased at the null point, $V_{DC}=V_{\pi\mathrm{DC}}$, the transfer function can be simplified as:

$$h\left[V_m(t)\right]=\sin\left[\frac{\pi}{2}\frac{V_m(t)}{V_{\pi\mathrm{RF}}}\right]\tag{8}$$

As the sine function is an odd function, the sign of the output

lightwave will follow the sign of the modulation voltage. In other words, when the modulation voltage goes through a zero-crossing, a phase shift of π will be introduced into the modulated light field. Thus, the PSK modulation of the probing pulse can be realized by applying modulation signals with the same magnitude but the opposite sign.

When the DC offset drift happens, $V_{DC} = V_{\pi\mathrm{DC}} + V_b$, where V_b is the bias drift. We mark the modulation voltage at the peak of the probing pulse as V_M and the intensity of the lightwave entering the MZM as I_0. As the intensity transfer function is the square of the lightwave transfer function's magnitude in Eq. (7), the output intensity of the paired pulses at the original peak position of the probing pulses can be expressed as:

$$I_{pi} = I_0 \sin^2\left[\frac{\pi}{2V_{\pi\mathrm{DC}}}V_b + (-1)^{i-1}\frac{\pi}{2V_{\pi\mathrm{RF}}}V_M\right] \quad (9)$$

When $|V_b/V_{\pi\mathrm{DC}}| + |V_M/V_{\pi\mathrm{RF}}| \le 1$, I_{p1} and I_{p2} represent the peak intensity of the probing pulses, as illustrated in Fig. 3(a) and (b).

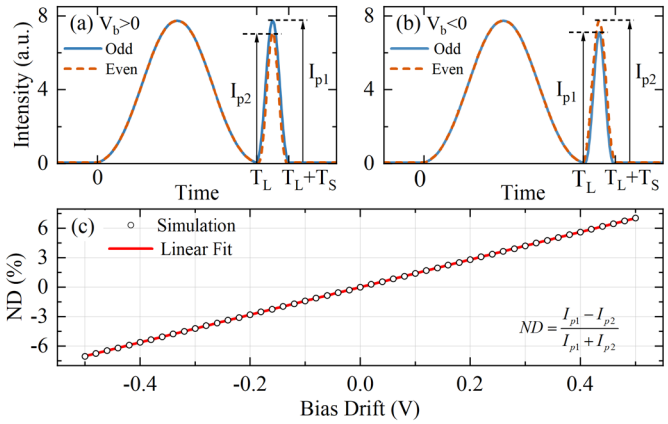

Fig. 3. Intensity envelopes of the modulated pulses at (a) 0.3 V (b) -0.1V bias drift. (c) The normalized difference (ND) of the probing pulses' peak intensity in simulation and its linear fit.

One can define the normalized difference (*ND*) of the paired pulses and obtain its small signal model as:

$$ND = \frac{I_{p1} - I_{p2}}{I_{p1} + I_{p2}} \approx \frac{\sin\left(\frac{\pi}{V_{\pi\mathrm{RF}}}V_M\right)}{1 - \cos\left(\frac{\pi}{V_{\pi\mathrm{RF}}}V_M\right)}\frac{\pi}{V_{\pi\mathrm{DC}}}V_b = k_d \cdot V_b \quad (10)$$

where k_d is the detection sensitivity of bias drift. Fig. 3(c) shows the *ND* in simulation with V_M, $V_{\pi\mathrm{RF}}$ and $V_{\pi\mathrm{DC}}$ of 5V, 6V and 6V, respectively. The good agreement of the simulated curve with its linear fit indicates that the *ND* can act as a linear sensor of the bias voltage. With a feedback control, the bias voltage can be maintained around zero.

III. Experiment

A. System Layout

The system layout of the proposed PSK-DCP lidar is shown in Fig. 4(a). A continuous-wave laser (CW, Amonics ALiDAR-150-Seed) is split into two parts, where the minor portion (5%) serves as the local oscillator (LO). The continuous seed is frequency shifted by 80 MHz and chopped into pulses with repetition rate of 25 kHz by an acousto-optic modulator (AOM). The pulse shaping and PSK modulation are both realized by an electro-optic MZM (iXblue MXER-LN-10). Fig. 4(b) illustrates the equally spaced paired pulse train.

A small portion (1%) of the modulated signal is detected by a photodetector (PD) to monitor the bias voltage of the MZM. In experiments, the MZM is biased at the null point. An erbium-doped fiber amplifier (EDFA, Amonics ALiDAR-150-AMP) is employed to amplify the paired pulses. In the receiver, the backscattered signal is mixed with the LO by a 50/50 beam splitter and down converted into electrical signal in IF band by beating on a balanced photodetector (BPD). After digitized by a 14-bit analog-to-digital converter (ADC), the raw data are stored in a computer for offline processing with the algorithm depicted in Section II. The AOM, MZM, and ADC are synchronized on a common reference provided by the arbitrary waveform generator (AWG, Keysight 33622A). The key system parameters are summarized in Table I.

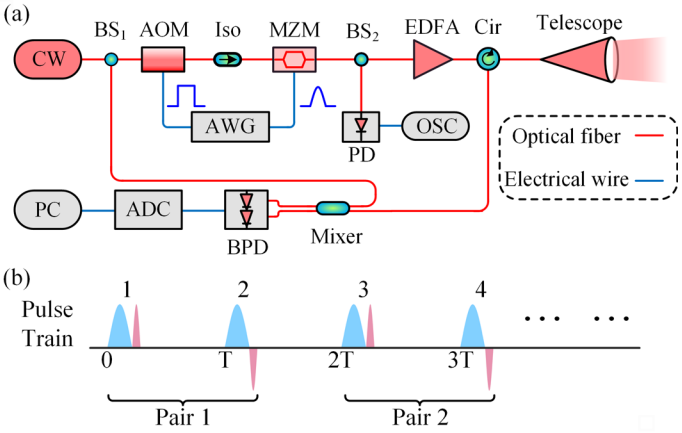

Fig. 4. (a) System layout of the PSK-DCP lidar. CW, continuous-wave laser; BS, beam splitter; Iso, isolator; AOM, acousto–optic modulator; Cir, circulator; PD, photodetector; BPD, balanced photodetector; ADC, analog-to-digital converter; AWG, arbitrary waveform generator; OSC, oscilloscope and PC, personal computer. (b) Transmitted pulse train in the pair method.

TABLE I
SUMMARY OF KEY SYSTEM PARAMETERS

Parameters	Value
Transmitter:	
Center wavelength	1550 nm
Pulse peak power	400 W
Pulse repetition rate	25 kHz
AOM frequency shift	80 MHz
MZM bandwidth	10 GHz
Transceiver:	
Telescope diameter	100 mm
Focal length	550 mm
Beam full divergence	44 μrad
Receiver:	
LO power	1.5 mW
Receiving bandwidth	200 MHz
Sample rate	500 MSps
Temporal resolution	0.1 s

B. Instrument Characterization

To get the detection sensitivity k_d of the bias drift under practical conditions, the normalized differences of probing pulses are measured at different bias voltages. The DC voltage on the MZM is changed from 5V to 6V and the *ND* is calculated from the observed intensity shapes. To distinguish the odd and even pulses, an extra trigger at the same repetition rate of the pulse pair is used. As shown in Fig. 5(a), the k_d is extracted from the slope of the linear fit of the measured data, with the R-squared parameter of this linear regression being 99.91%.

Fig. 5 (b) shows a continuous monitoring of the bias drift for 16 s. The refresh time interval of the bias detection is set to be 20 ms, averaging on 250 pulse pairs. Intentional disturbances are applied in a step of 0.1 V, which is well followed by the bias detector.

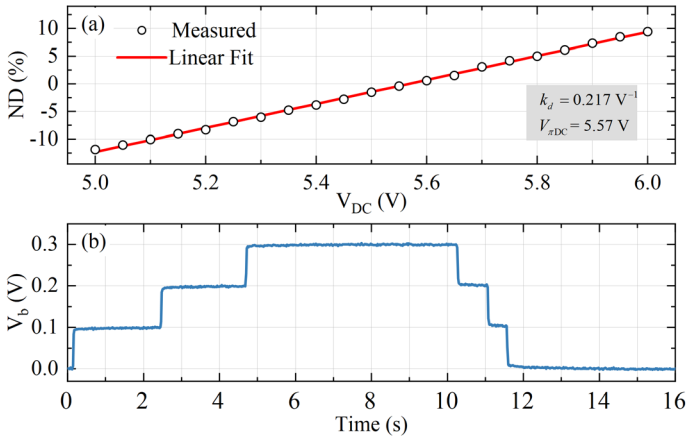

Fig. 5. (a) Measured *ND* of the probing pulses in the experiment and its linear fit. (b) Real-time monitoring of the bias drift under intentional disturbance.

When the MZM is biased at the null point, the modulated lightwave is observed through homodyne detection with a 180° optical hybrid. As an example, Fig. 6(a) shows the electric field's amplitude envelope of the paired pulses before amplification, where the truncated lengths of A_L and A_S are 200 ns and 30 ns, respectively. The half widths at exp(-0.5) of the common pulse (σ_c) and probing pulse (σ_p) are 50 ns and 8 ns. The peak magnitude of the probing pulse is designed to be slightly higher than the common pulse to reduce their intensity difference after amplification [28]. As shown Fig. 6(b), the intensity envelopes of the amplified odd and even pulses are quite close. The full width at half-maximum (FWHM) pulse durations of the common pulse (τ_c) and probing pulse (τ_p) are measured to be 85 ns and 13 ns. As to the receiver, since the power of the LO is as high as 1.5 mW, it is operating at the shot noise limit [29].

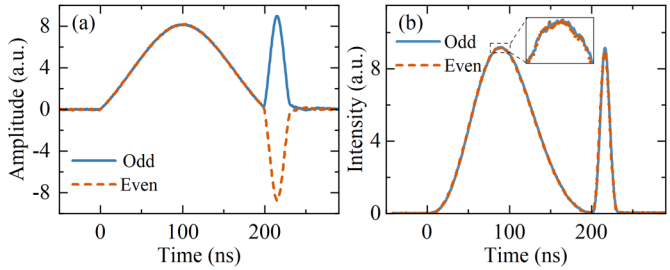

Fig. 6. (a) The lightwave envelope of the odd and even pulses modulated by the MZM. (b) The intensity of the amplified pulse pair.

C. Wind Profiling Results

During the experiments, the system is placed on the 9th floor of the laboratory building (32.20°N, 118.72°E) with the telescope pointing to the south at an elevation angle of 15°. In the data processing, window functions matched to the amplitude envelopes of the common and probing pulses are used to achieve optimum receiving [30]. As the half widths at exp(-0.5) of the probing pulse's amplitude envelope and the corresponding window function are both 8 ns, a spatial resolution of 3 m is realized according to Eq. (6). It is noted that the Eq. (6) has been verified in the experiment [24]. The temporal resolution is set as 0.1 s in this work, averaging the backscattered spectra of 1.25k pulse pairs. For each spectrum, the fast Fourier transform (FFT) length is extended to 4096 through zero padding.

As a reference, the atmospheric echoes of the odd pulses are regarded as the backscattered signals got by a conventional CDWL with low spatial resolution. Since the conventional pulsed CDWL accumulates the backscattering spectrum of each single pulse (SP) rather than pair, it would be called as SP Ref for brevity. The consistency with SP Ref is a necessary condition for the validity of the proposed lidar's measurement. As it's difficult to directly get the uncertainties of a wind lidar in such a high resolution due to the lack of calibrated references [28], the standard deviation (SD) of the velocity would be preliminarily estimated by the Cramer-Rao lower bound (CRLB) [31],[32]. While the center frequency is estimated by Gaussian fitting with trust-region algorithm here, the CRLB provides a lower bound of the estimation uncertainty [28].

In a first wind profiling experiment, measurement results are plotted in Fig. 7, where the blue solid line and black dash line stand for the PSK-DCP and SP Ref, respectively.

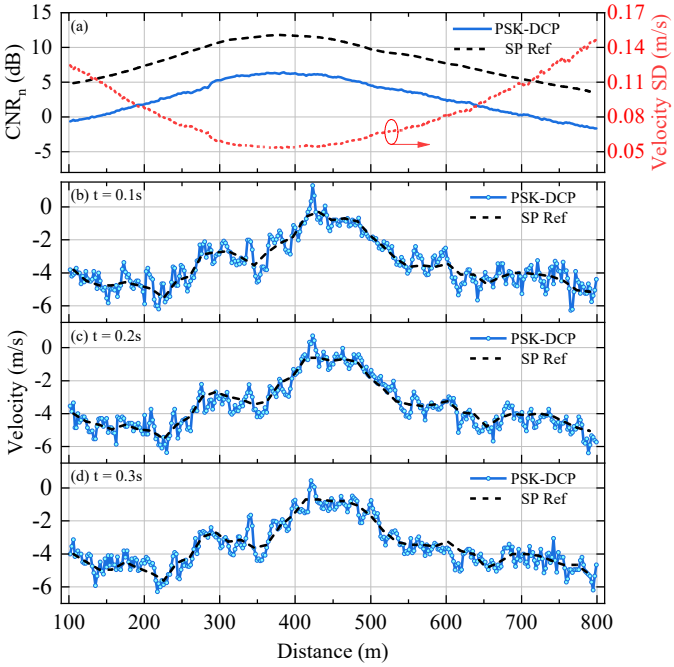

Fig. 7. (a) Narrowband CNR and corresponding CRLB. (b)-(d) Radial wind velocity profiles of the PSK-DCP lidar and the SP reference with temporal resolution of 0.1 s.

The velocity SD of the PSK-DCP lidar is derived from the

narrowband carrier-to-noise ratio (CNR_n) [31], as shown by the red dot line in Fig. 7 (a). The CNR_n is defined in the spectral domain as the signal power divided by the noise power under the 1/e full width of the signal peak. The trend of CNR_n versus distance is related to many factors, including the system configuration (like the focal length) and the weather condition (like the visibility). It can be observed that the SD of the velocity doesn't exceed 0.15 m/s within 800 m.

In a continuous measurement for 0.3 s, the wind velocity profiles of the two methods have the same trend versus distance, as shown in Fig. 7(b-d). The profile got by the high-spatial-resolution PSK-DCP lidar changes continuously around that of the SP Ref. There are some differences between the two sets of profiles at some distances (like 420 m and 618 m), which can be attributed to the smoothing effect caused by the low spatial resolution of the SP Ref. The backscattered spectra at these distances are shown in Fig. 8. One can observe that the PSK-DCP method basically avoids the spectrum broadening while achieving high spatial resolution. Though the CNR_n of the PSK-DCP is lower compared with the SP Ref due to the high spatial resolution, the signal peaks can still be discriminated from the noise effectively.

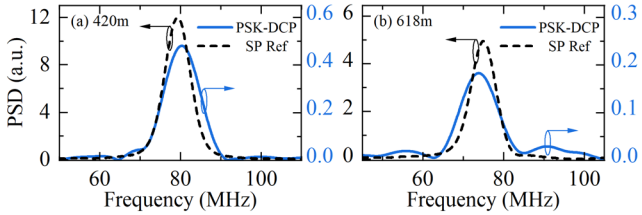

Fig. 8. Spectra of the PSK-DCP lidar and the SP reference at (a) 420 m and (b) 618 m.

A second experiment was carried out on 16 March 2022. While a cold wave went through the East China, the temperature dropped by 20 ℃ (from 29 ℃ to 9 ℃) in one day. During the severe convective weather caused by the strong cold air, the wind field may change greatly in a relatively small temporal and spatial scale. As an initial prototype, the system cannot store long-term measurement results, limited by the huge amount of raw data. Therefore, a continuous observation for 8 s was conducted at 19:30 local time. As shown in Fig. 9, the evolution of the wind field is profiled with a spatial/temporal resolution of 3 m/0.1 s. In the experiment, continuous structures of the wind field can be observed. For instance, a band with positive wind velocity exists for over 6 s around 650 m away. One possible cause for the layering can be the gradient distribution of air temperature near the ground related to the sudden drop of temperature. This continuity conforms the time-varying characteristics of the wind field, which further verifies the reliability of the measurement.

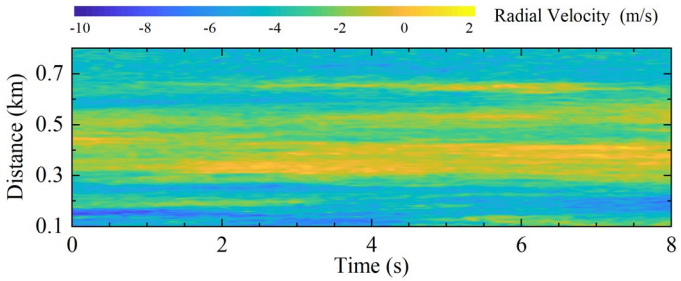

Fig. 9. Continuous radial wind profiles for 8 s with spatial/temporal resolution of 3 m/0.1 s

IV. Discussion

Different from the previous work where only one probing pulse is included in the pulse pair [24], the PSK-DCP method employs two probing pulses with π-phase shift in pair. Therefore, the total energy of the probing pulses doubles, as well as the CNR_n [19]. Another benefit from the PSK modulation is on the waveform control. When the EDFA is uniformly pumped, pulses with different intensity envelope will be amplified with different gains. To neutralize the time-dependent gain profile of the amplifier, the modulating signals need to be particularly designed to minimize the difference between the amplified common parts in one pulse pair [24]. Moreover, the design varies on different environment and amplifiers, which increases the difficulty of system deployment. In the PSK-DCP method, benefiting from the identical intensity envelope of the paired pulses (Fig. 6(b)), the problem above can be avoided. By equally spacing the pulses with identical intensity envelope, the system is less sensitive to the gain profile of the EDFA, thus reducing the difficulty of waveform control and improving the robustness against environmental disturbance.

In the proposed method, while the duration of the probing pulse is directly related to the spatial resolution, the duration of the common pulse is flexible. Although a longer common pulse can reduce the spectral width by extending the effective duration of R_d as explained in Section II.A, some negative effects will also be introduced. Firstly, the long specular reflection from the output optics in a monostatic configuration will increase the blind area [28]. Secondly, a longer common pulse may reduce the CNR_n by increasing the variance of the R_d. It is noted that the expectation value of the cross-correlation of backscattered signals from different distances is zero, but the variance always exists. To optimize the system performance, trade-offs need to be made.

V. Conclusion

A coherent Doppler wind lidar based on DCP technique incorporating PSK modulation is proposed and experimentally demonstrated. The principle of the PSK-DCP method is explained in detail through theoretical analysis and numerical simulation. In experiments, the binary PSK modulation together with the pulse shaping is realized by an MZM with real-time bias monitoring. At laser peak power of 400 W, continuous radial wind profiling over 800 m is demonstrated with the spatial and temporal resolution of 3 m and 0.1 s,

respectively.

Considering that the high-speed signal processing has been realized by a field-programmable-gate-array (FPGA) in real time [33], the limitation of data storage on continuous observation duration could be greatly alleviated. To further demonstrate the role of the high resolution CDWL in aerodynamic structure observation, a measurement of the aircraft wake vortices is under preparing. The retrievals based on spectrum analysis [11] would be used to deal with the spectral deformation caused by the rapid dynamic process.

APPENDIX: Numerical Simulation of F_{LS}

The truncated Gaussian function used in the simulation is formed by truncating a Gaussian function at the point where the intensity falls to 10% of its peak and shifting the DC level to the truncated point to avoid discontinuity. A truncated Gaussian function with truncated length of 200 ns is used for the amplitude envelope of the common pulse $A_L(t)$ and the long window function $W_L(t)$. Another truncated Gaussian function with truncated length of 30 ns is used for the amplitude envelope of the probing pulse $A_S(t)$ and the short window function $W_S(t)$. The $F_{LS}(\delta z,\tau)$ is defined as:

$$F_{LS}(\delta z,\tau)=\int A_L(t-\delta t)A_S(t-\delta t+\tau)W_L(t)W_S(t+\tau)dt \quad (11)$$

The variables are meshed by the parameters shown in Table II, and the values of the $F_{LS}(\delta z,\tau)$ at the 2D grid are calculated by numerical integral. The result has been shown in Fig. 2.

TABLE II
GRID PARAMETERS FOR THE SIMULATION

	Range	Grid Interval
Temporal:		
τ	[0,230 ns]	
δt	[-30 ns, 30 ns]	0.2 ns
t	[0,200 ns]	
Spatial:		
δz	[-4.5 m, 4.5 m]	0.03 m

To clarify the spatial resolution of the DCP method, the contribution of the signals from different δz to the $R_d(\tau,t_0)$ is analyzed base on the Eq. (5). Assuming that the $\beta(z_0+\delta z)$ keeps unchanged when δz is in the range of a few meters, the power of each complex exponential function $\exp\{-j2\pi[f_{IF}+f_d(z_0+\delta z)]\tau\}$ is determined by the square of its amplitude envelope, which is $F_{LS}^2(\delta z,\tau)$. Thus, the energy proportion (p_E) of the backscattered signal from a cell within range z_c can be got by:

$$p_E=\frac{\int_{-z_c/2}^{z_c/2}\int_{-\infty}^{\infty}F_{LS}^2(\delta z,\tau)d\tau d(\delta z)}{\int_{-\infty}^{\infty}\int_{-\infty}^{\infty}F_{LS}^2(\delta z,\tau)d\tau d(\delta z)} \quad (12)$$

As shown in Fig. 10, 87% energy of the differential cross correlation $R_d(\tau,t_0)$ is contributed by signals from a range cell of 3 m. The result is consistent with the spatial resolution calculated by the Eq. (6).

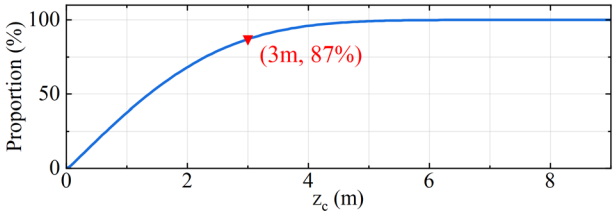

Fig. 10 Energy proportion of the signals from cells with different sizes.

REFERENCES

[1] B. Witschas, S. Rahm, A. Dörnbrack, J. Wagner, and M. Rapp, "Airborne Wind Lidar Measurements of Vertical and Horizontal Winds for the Investigation of Orographically Induced Gravity Waves," *J. Atmos. Ocean. Technol.,* vol. 34, no. 6, pp. 1371-1386, Jun. 2017.

[2] M. Jia *et al.*, "Long-lived high-frequency gravity waves in the atmospheric boundary layer: observations and simulations," *Atmos. Chem. Phys.,* vol. 19, no. 24, pp. 15431-15446, Dec. 2019.

[3] Y. Yang *et al.*, "Diurnal Evolution of the Wintertime Boundary Layer in Urban Beijing, China: Insights from Doppler Lidar and a 325-m Meteorological Tower," *Remote Sens.,* vol. 12, no. 23, Dec. 2020, Art. no. 3935.

[4] Y. Chu *et al.*, "Characterizing warm atmospheric boundary layer over land by combining Raman and Doppler lidar measurements," *Opt. Express,* vol. 30, no. 7, pp. 11892-11911, Mar. 2022.

[5] Y. Käsler, S. Rahm, R. Simmet, and M. Kühn, "Wake Measurements of a Multi-MW Wind Turbine with Coherent Long-Range Pulsed Doppler Wind Lidar," *J. Atmos. Ocean. Technol.,* vol. 27, no. 9, pp. 1529-1532, Sep. 2010.

[6] M. A. Mohandes and S. Rehman, "Wind Speed Extrapolation Using Machine Learning Methods and LiDAR Measurements," *IEEE Access,* vol. 6, pp. 77634-77642, Dec. 2018.

[7] N. J. Harvey, R. J. Hogan, and H. F. Dacre, "Evaluation of boundary-layer type in a weather forecast model utilizing long-term Doppler lidar observations," *Q. J. R. Meteorol. Soc.,* vol. 141, no. 689, pp. 1345-1353, Apr. 2015.

[8] Y. Yang *et al.*, "Characteristics of Heavy Particulate Matter Pollution Events Over Hong Kong and Their Relationships With Vertical Wind Profiles Using High-Time-Resolution Doppler Lidar Measurements," *J. Geophys. Res.: Atmos.,* vol. 124, no. 16, pp. 9609-9623, Dec. 2019.

[9] T. Huang *et al.*, "Assessing Transboundary-Local Aerosols Interaction Over Complex Terrain Using a Doppler LiDAR Network," *Geophys. Res. Lett.,* vol. 48, no. 12, Jun. 2021, Art. no. e2021GL093238.

[10] T. Wei, H. Xia, B. Yue, Y. Wu, and Q. Liu, "Remote sensing of raindrop size distribution using the coherent Doppler lidar," *Opt. Express,* vol. 29, no. 11, pp. 17246-17257, May. 2021.

[11] J. Yuan, H. Xia, T. Wei, L. Wang, B. Yue, and Y. Wu, "Identifying cloud, precipitation, windshear, and turbulence by deep analysis of the power spectrum of coherent Doppler wind lidar," *Opt. Express,* vol. 28, no. 25, pp. 37406-37418, Dec. 2020.

[12] J. Yuan *et al.*, "Cloud Seeding Evidenced by Coherent Doppler Wind Lidar," *Remote Sens.,* vol. 13, no. 19, Sep. 2021, Art. no. 3815.

[13] I. N. Smalikho and V. A. Banakh, "Estimation of aircraft wake vortex parameters from data measured with a 1.5um coherent Doppler lidar," *Opt. Lett.,* vol. 40, no. 14, pp. 3408-3411, Jul. 2015.

[14] J. N. Hallock and F. Holzäpfel, "A review of recent wake vortex research for increasing airport capacity," *Progress in Aerospace Sciences,* vol. 98, pp. 27-36, Mar. 2018.

[15] S. Wu, X. Zhai, and B. Liu, "Aircraft wake vortex and turbulence measurement under near-ground effect using coherent Doppler lidar," *Opt. Express,* vol. 27, no. 2, pp. 1142-1163, Jan. 2019.

[16] I. N. Smalikho, V. A. Banakh, F. Holzäpfel, and S. Rahm, "Method of radial velocities for the estimation of aircraft wake vortex parameters from data measured by coherent Doppler lidar," *Opt. Express,* vol. 23, no. 19, pp. A1194-A1207, Sep. 2015.

[17] V. Banakh and I. Smalikho, *Coherent Doppler Wind Lidars in a Turbulent Atmosphere*. Norwood, MA, USA: Artech House, 2013, pp. 41-48.

[18] R. G. Frehlich and M. J. Yadlowsky, "Performance of Mean-Frequency Estimators for Doppler Radar and Lidar," *J. Atmos. Ocean. Technol.,* vol. 11, no. 5, pp. 1217-1230, Oct. 1994.

[19] S. W. Henderson, P. Gatt, D. Rees, and R. M. Huffaker, "Wind Lidar," in *Laser remote sensing*, T. Fujii and T. Fukuchi Eds. Boca Raton, FL, USA: CRC, 2005, ch. 7, pp. 520-523.

[20] C. Liang, C. Wang, X. Xue, X. Dou, and T. Chen, "Meter-scale and sub-second-resolution coherent Doppler wind LIDAR and hyperfine wind observation," *Opt. Lett.,* vol. 47, no. 13, pp. 3179-3182, Jul. 2022.

[21] X. Rui, P. Guo, H. Chen, S. Chen, and Y. Zhang, "Adaptive iteratively reweighted sine wave fitting method for rapid wind vector estimation of pulsed coherent Doppler lidar," *Opt. Express,* vol. 27, no. 15, pp. 21319-21334, Jul. 2019.

[22] N. Prasad, R. Sibell, S. Vetorino, R. Higgins, and A. Tracy, "An all-fiber, modular, compact wind lidar for wind sensing and wake vortex applications," in *SPIE Defense + Security*, 2015, vol. 9465, 94650C, doi: 10.1117/12.2181170.

[23] Y. Zhang, Y. Wu, and H. Xia, "Spatial Resolution Enhancement of Coherent Doppler Lidar by Pseudo-Random Phase Coding," *J. Lightwave Technol.,* vol. 40, no. 13, pp. 4467-4473, Jul. 2022.

[24] Y. Zhang, Y. Wu, and H. Xia, "Spatial resolution enhancement of coherent Doppler wind lidar using differential correlation pair technique," *Opt. Lett.,* vol. 46, no. 22, pp. 5550-5553, Nov. 2021.

[25] T. Horiguchi, Y. Masui, and M. S. D. Zan, "Analysis of Phase-Shift Pulse Brillouin Optical Time-Domain Reflectometry," *Sensors,* vol. 19, no. 7, Mar. 2019, Art. no. 1497.

[26] D. Ba, Y. Li, J. Yan, X. Zhang, and Y. Dong, "Phase-coded Brillouin optical correlation domain analysis with 2-mm resolution based on phase-shift keying," *Opt. Express,* vol. 27, no. 25, pp. 36197-36205, Dec. 2019.

[27] P. Salamitou, A. Dabas, and P. H. Flamant, "Simulation in the time domain for heterodyne coherent laser radar," *Appl. Opt.,* vol. 34, no. 3, pp. 499-506, Jan. 1995.

[28] P. Schroeder, W. A. Brewer, A. Choukulkar, A. Weickmann, and S. Sandberg, "A Compact, Flexible, and Robust Micropulsed Doppler Lidar," *J. Atmos. Ocean. Technol.,* vol. 37, no. 8, pp. 1387-1402, Aug. 2020.

[29] K. Kikuchi, "Fundamentals of Coherent Optical Fiber Communications," *J. Lightwave Technol.,* vol. 34, no. 1, pp. 157-179, Jan. 2016.

[30] J. G. Proakis and M. Salehi, "Optimum Receivers for AWGN Channels," in *Digital Communications*, 5 ed. New York, NY, USA: McGraw-Hill Education, 2007, ch. 4, pp. 178-182.

[31] B. J. Rye and R. M. Hardesty, "Discrete spectral peak estimation in incoherent backscatter heterodyne lidar. I. Spectral accumulation and the Cramer-Rao lower bound," *IEEE Geosci. Remote Sens. Lett.,* vol. 31, no. 1, pp. 16-27, Jan. 1993.

[32] S. W. Henderson, P. Gatt, D. Rees, and R. M. Huffaker, "Wind Lidar," in *Laser remote sensing*, T. Fujii and T. Fukuchi Eds. Boca Raton, FL, USA: CRC, 2005, ch. 7, pp. 550-570.

[33] O. Kliebisch and P. Mahnke, "Real-time laser Doppler anemometry for optical air data applications in low aerosol environments," *Rev. Sci. Instrum.,* vol. 91, no. 9, May 2020, Art. no. 095106.